Flow mechanisms of leading-edge-tubercled hydrofoils and their implications for ship propulsion and underwater noise

Chengyi Zhou[a], Robiya Nabijonova[a], Danlei Yang[a, b, *], Blanca Pena[a], Tim Wood[c], Luofeng Huang[a, *]

[a]Faculty of Engineering and Applied Sciences, Cranfield University, Cranfield, MK43 0AL, United Kingdom

[b]Department of Engineering, City St George's University of London, London, EC1V 0HB, United Kingdom

[c]Achelous Energy Limited, Unit 2 Black Robins Farm, Edenbridge TN8 6QP, United Kingdom

Corresponding authors: danlei.yang@citystgeorges.ac.uk (D.Yang); luofeng.huang@cranfield.ac.uk (L. Huang)

Abstract

Upstream hydrofoils modify the flow approaching a ship propeller, but their hydrodynamic and acoustic consequences depend on how the induced vortices, separation and pressure fluctuations interact with the downstream system. This study combines (a) a computational investigation of isolated tubercled hydrofoils with (b) towing-tank experiments on hydrofoils mounted ahead of a model tanker propeller. An unsteady Reynolds-averaged Navier–Stokes campaign covered 31 hydrofoil geometries at seven angles of attack and a Reynolds number of 1.83×10^5. The computed flow exhibits counter-rotating streamwise vortices and an incidence-dependent transition from localised separation to a connected separated region. The experiments assessed 30 hydrofoil configurations using hydrophone pressure spectra and distance per revolution (DPR). The largest single-band pressure power spectral density reduction was 80.2%, while the highest configuration-mean DPR increased by 7.8%; these are separate outcomes and do not establish simultaneous gains. Tubercle effects changed sign with the underlying geometry. Integrating the computational and experimental analysis, the studies support a framework in which upstream flow restructuring produces geometry-dependent hydrodynamic–acoustic trade-offs. The paper shows a series of insights that tubercled hydrofoils can generate counter-vortex flows and this can generate notable implications in ship hydrodynamics and underwater noise control.

Keywords: Leading-edge tubercles; hydrofoil; streamwise vortices; propeller inflow; pressure fluctuations; underwater noise.

Nomenclature

$\boldsymbol{A}$	amplitude (peak-to-trough distance)
a	Numerical sinusoidal amplitude; numerical peak-to-trough distance = 2a
ANOVA	analysis of variance
AOA	angle of attack
C	chord length
$\mathcal{C}$	set of the three non-target design parameters used for adjustment
CAD	computer-aided design
CFD	computational fluid dynamics
C_L, C_D	Lift and drag coefficients of the isolated numerical hydrofoil
CV	coefficient of variation
d	target design parameter in the net effect analysis
d_i	level of the target parameter for configuration i
DPR	distance per revolution
e_i	regression residual for configuration i
$\bar{e}_\ell$	mean residual at level ℓ (estimated net effect)
F	ANOVA F-statistic
f	frequency
Fr	Froude number
g	group index in the one-way ANOVA
G_f	sound pressure power spectral density at frequency f ($\mu Pa^2/Hz$)
i, j	configuration index and adjustment-factor index, respectively
IDDES	Improved delayed detached-eddy simulation
IMO	International Maritime Organization
ITTC	International Towing Tank Conference
k	number of factor levels in the one-way ANOVA
KVLCC	Korean Very Large Crude Carrier

ℓ	level of the target design parameter
ℓ_a, ℓ_b	two factor levels compared in the t-test
L/D	Isolated-hydrofoil lift-to-drag ratio
LET	Leading-edge tubercle
L_p	sound pressure spectral density level
N	number of tubercles
n	total sample size used in the analysis
n_g	number of observations in group g
n_ℓ	number of configurations at level ℓ
NoBlade	static test with a blade-less dummy propeller
P	position of hydrofoil
p	statistical p-value
PLA	polylactic acid
p_{ref}	reference sound pressure (1 μPa)
p′rms	Area-weighted mean of local temporal surface-pressure RMS (Pa)
Re	Reynolds number
RegularDy	dynamic test with the regular propeller
RegularSt	static test with the regular propeller
RPS	propeller rotational speed in revolutions per second
s, S, Sf	Numerical foil span, planform area and wetted surface area
s^2_ℓ	sample variance of residuals at level ℓ
SD	standard deviation
SS	sum of squares
$SS_{between}$	between-group sum of squares
SS_{within}	within-group sum of squares
STFT	short-time Fourier transform
t	two-sample t-statistic

U	vessel advance velocity
$U\infty$	Numerical freestream velocity
URANS	Unsteady Reynolds-averaged Navier–Stokes
W	wingspan length
X_0	chordwise coordinate on the original hydrofoil profile
$x_{i,j}$	level of parameter j for configuration i
X_{mod}	chordwise coordinate on the modified peak profile
$\bar{y}$	overall mean response
$\bar{y}_g$	mean response in group g
y_{gi}	observation i in group g
y_i	response of configuration i
α	Numerical angle of attack
β_0	regression intercept
β_j	regression coefficients for parameter j
λ	wavelength
μ	mean of repeated measurements
σ	standard deviation of repeated measurements

1 Introduction

Reducing the energy demand and underwater noise of shipping requires an understanding of how the flow around a vessel interacts with its propulsion system. Underwater noise can arise from machinery, propeller loading, cavitation and hull-related flow, and its environmental effects have motivated international mitigation guidance [1,2,3]. The International Maritime Organization (IMO) greenhouse-gas strategy provides a parallel motivation for improving propulsion performance [4]. A hydrofoil mounted upstream of a propeller offers a passive means of changing the incoming flow, but any benefit must be assessed against the drag and unsteady disturbances introduced by the hydrofoil itself. The leading-edge tubercles of humpback-whale flippers (Figure 1) provide one approach to controlling this flow through three-dimensional vortex structures [5].



Figure 1. Humpback whales' tubercled flippers (Source: Wikimedia Commons, under CC BY license) [6]

Leading-edge tubercles (LETs) generate spanwise variations in pressure and counter-rotating streamwise vortices that redistribute momentum and modify separation. Early work by Watts and Fish [7] established their potential to change lifting-surface performance. Experiments on National Advisory Committee for Aeronautics (NACA) 63$_4$-021 foils showed that the response depends strongly on tubercle amplitude and incidence, with different consequences before and after stall [8]. Fan et al. [9] examined alternative leading-edge constructions and identified the role of vortex pairs in post-stall flow control. At lower Reynolds number, Wei et al. [10,11] linked reduced separation to increased unsteadiness for some amplitude-to-wavelength ratios. Finite-span experiments also demonstrate that amplitude, wavelength and aspect ratio influence the response [12]. These findings motivate analysis of the actual vortex and separation structures rather than treating tubercles as a uniformly beneficial modification. Numerical modelling provides access to these structures, but the turbulence closure and

sampling duration constrain their interpretation. Pena et al. [13] used improved delayed detached-eddy simulation (IDDES) to analyse a NACA 63_4-021 tubercled hydrofoil.

Studies distinguish the effects of tubercles on mean loading from the mechanisms that generate three-dimensional flow. Miklosovic et al. [14] measured an approximately 40% increase in stall angle for an idealised humpback-flipper model with tubercles, establishing a benefit for that finite-span geometry rather than a universal performance gain. Rostamzadeh et al. [15] combined lifting-line arguments, wind-tunnel measurements and transitional unsteady Reynolds-averaged Navier–Stokes calculations for NACA 0021-based foils; their results associated undulating leading edges with spanwise circulation variations and a pair of streamwise vortices per wavelength. Their subsequent experimental and numerical study [16] identified a skew-induced vortex-formation mechanism and showed that primary and secondary vortices enhanced momentum transfer and reduced separation after stall, whereas the modification penalised pre-stall performance.

The persistence of tubercle-induced structures into a propulsion-system wake is a separate question. Large-eddy simulations by Posa et al. [17] showed that leading-edge tubercles on propeller blades redistributed suction-side pressure minima and generated streamwise vortices, without generally improving propulsive efficiency. These vortices broke up early, leaving the main wake dynamics dominated by tip and hub vortices. Although their geometry differs from a stationary hydrofoil upstream of a propeller, the result cautions against inferring a sustained downstream flow modification from near-surface vortex formation alone; the structures' development distance and interaction with the receiving flow must also be considered.

The acoustic consequences of flow control require separate consideration from the mean forces. Hansen et al. [18] demonstrated tonal-noise reduction with leading-edge tubercle modifications, while studies of propellers show that noise and efficiency can form competing objectives [19]. Pressure-field analysis and model-scale measurements help characterise propulsion noise [20,21,22], but local pressure fluctuations and radiated sound are different quantities. Surface loading acts as an acoustic source [23], while its temporal and spatial coherence affects radiation [24]. An area-averaged surface pressure RMS can therefore compare fluctuation levels within a numerical campaign, but cannot be converted directly into a hydrophone spectral level or a far-field noise reduction.

A direct hydroacoustic extension was provided by Posa et al. [25], who combined large-eddy simulation with the Ffowcs Williams–Hawkings acoustic analogy for conventional and tubercled propellers in wetted conditions. Tubercles substantially altered blade-surface pressure fluctuations and loading sound, while the wake-related quadrupole contribution changed

comparatively little. Loading sound decreased near the blade frequency but increased around ten times that frequency. This frequency-dependent response demonstrates why neither a change in mean loading nor a single surface-pressure RMS value establishes broadband noise reduction. It supports interpreting the present measurements through geometry-dependent changes in flow structures and pressure spectra, while keeping local hydrodynamic pressure distinct from radiated sound.

Marine applications include tubercled ducts, propellers and tidal-turbine blades. Stark et al. [26] found geometry- and operating-condition-dependent changes in the forces of a ducted propeller, while Shi et al. [27] investigated tubercled tidal-turbine blades. These applications differ from fitting a separate hydrofoil ahead of a ship propeller. Hull-form and appendage changes offer additional routes to modifying vessel performance [28,29]. For upstream devices specifically, Guo et al. [30] used stereoscopic particle image velocimetry to examine how a pre-swirl stator changes the propeller inflow. This establishes the relevance of measuring the velocity field at the propeller plane. However, a designed pre-swirl distribution cannot be inferred merely from the presence of alternating local vortex pairs behind a tubercled hydrofoil.

The unresolved question is how hydrofoil-induced flow restructuring relates to the hydrodynamic and acoustic response of a downstream propulsion system. This paper addresses that question through two complementary investigations. First, the isolated-foil calculations resolve the relationship between geometry, incidence, separation, vortical structures and surface pressure fluctuations. Second, towing-tank experiments assess smooth and tubercled hydrofoils upstream of a KVLCC2-type model tanker propeller using DPR and underwater pressure spectra. The studies use different foil sections, Reynolds numbers and boundary conditions; they are therefore interpreted together at the mechanism level. The central hypothesis is that hydrofoil-generated vortices and crossflow interact with coherent hull-wake structures before they reach the propeller, potentially weakening or redirecting adverse inflow disturbances and changing blade loading. The paper is structured as follow: Section 2 presents the Computational Fluid Dynamics (CFD) methodology and flow analysis. Section 3 presents the ship-model experimental methods and results. Section 4 integrates the evidence into a physical interpretation of upstream flow control and identifies future work. Section 5 gives the combined conclusions.

2 Computational investigation of hydrofoil flow mechanisms

2.1 Hydrofoil geometry and computational conditions

The baseline section is NACA 63_4-021 with nominal chord C = 100 mm and span s = 300 mm. A sinusoidal leading edge is used while the trailing edge remains straight (Figure 2). To distinguish the numerical convention from the experimental peak-to-trough distance A, the numerical sinusoidal amplitude is denoted a throughout this paper. The leading-edge coordinate is $x_{LE}(z) = -a\cos(2\pi z/\lambda)$, and the local chord is $c(z) = C + a\cos(2\pi z/\lambda)$. Thus, the numerical peak-to-trough distance is 2a. The reference tubercled foil has a/C = 0.10 and λ/C = 0.50; it is not a smooth-foil reference.

Thirty geometries were sampled by Latin hypercube sampling over a/C = 0.02–0.15 and nominal λ/C = 0.15–0.50, giving 31 geometries including the reference. The wavelengths were adjusted to fit an integer number of half-waves across the span, with a maximum adjustment of 3.4%; the as-built wavelength was used in the analysis. Each geometry was evaluated at α = 0°, 5°, 10°, 15°, 20°, 25° and 30°. Water entered at U_∞ = 1.837 m/s, giving Re = 1.83×10^5 based on C. The inlet turbulence intensity was 1% and the turbulent viscosity ratio was 10.

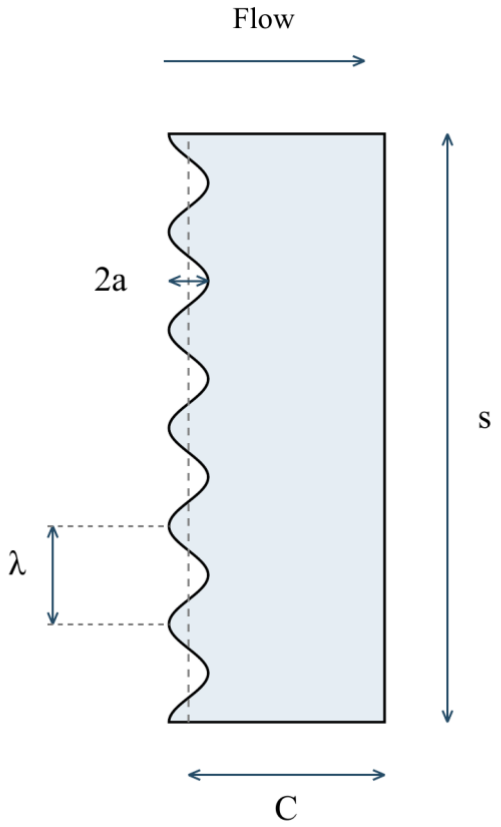


Figure 2. Plan view of the numerically tested tubercled hydrofoil, illustrating the leading-edge geometry: nominal chord C, span s, wavelength λ and peak-to-trough distance 2a.

The computational domain extended 15C upstream, 20C downstream and 10C to each lateral boundary (Figure 3). A velocity inlet and pressure outlet were imposed, with a no-slip foil surface and symmetry conditions at the two spanwise boundaries. Leading-edge peaks or troughs coincided with those span boundaries. Consequently, the calculations do not represent the free wing tips of the small ship-mounted hydrofoils. Force coefficients were defined using $S = Cs = 0.03\ m^2$: $C_L = L/(\frac{1}{2}\rho U_\infty^2 S)$ and $C_D = D/(\frac{1}{2}\rho U_\infty^2 S)$, with $L/D = C_L/C_D$ used as the foil performance measure.

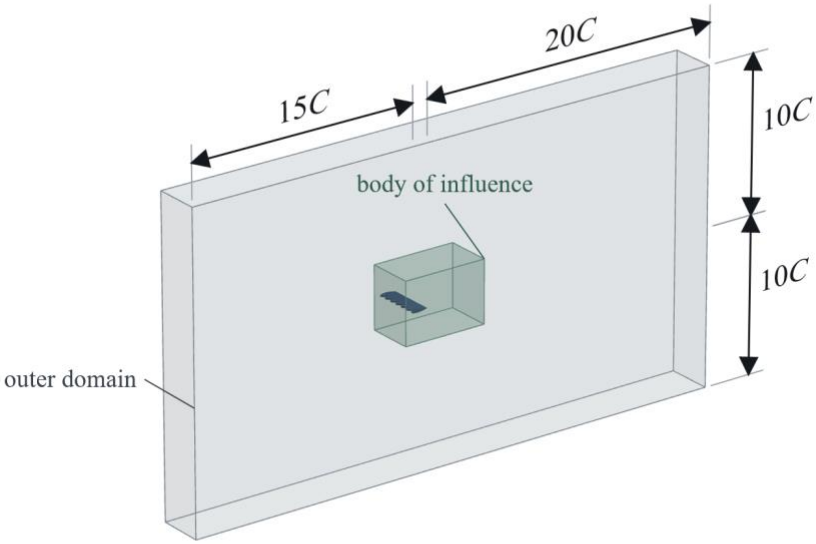


Figure 3. Computational domain and local mesh-refinement region for the isolated hydrofoil. C is the nominal chord.

2.2 Mesh solver and pressure-fluctuation measure

Meshes were generated in ANSYS Fluent Meshing 2025 R2 using a consistent watertight-geometry workflow. The poly-hexcore meshes contained 12.38–12.55 million cells, with 25 prism layers, a surface target size of 0.0215C and a first-cell height of 10^{-4}C, giving y^+ of order unity or below on the fine mesh. A refinement region covered $-0.5C \le x \le 5C$ and $-2C \le y \le 2C$. A three-mesh sensitivity study at 20° used approximately 3.08, 6.19 and 12.4 million cells. The reported coefficient spreads were 3.7% for lift and 1.1% for drag; the fine mesh was selected.

The pressure-based Fluent solver used second-order spatial discretisation and the four-equation transition SST model [31,32]. A steady RANS stage of up to 300 iterations preceded the URANS stage. The latter used second-order implicit time stepping, $\Delta t = 2.5$ ms and 20 inner iterations per step. The first 360 unsteady steps were discarded, followed by at most 900 sampling steps. The stopping criterion used a relative change in block-mean lift below 0.5% for two successive 370-step comparisons, subject to the sampling cap. Force means were evaluated over the final sampling block. These settings are retained as the provenance of the numerical results, not as evidence of temporal convergence.

The pressure-fluctuation measure is the area-weighted mean of the local temporal RMS over the wetted foil surface: $p'_{rms} = (1/Sf) \int_{Sf} \sqrt{\langle (p - \langle p \rangle)^2 \rangle}\, dS$, where Sf is surface area and angle brackets denote temporal averaging. It is reported in Pa and differs from the RMS of an area-integrated pressure signal. It retains local fluctuation amplitudes but not their phase relationships, and is used only as a comparative loading-fluctuation measure. No acoustic propagation, FW-H calculation or cavitation model is used; p'_{rms} is therefore not a predicted radiated sound-pressure level [23,24].

2.3 Separation and streamwise vortex structures

The reference-foil flow changes markedly with incidence. At 5°, reversed near-wall flow is localised mainly behind the troughs, with attached lanes behind the leading-edge peaks. At 10°, the separated patches expand and connect; by 25°, reversal covers most of the suction side, interrupted by a remaining attached region (Figure 4). The pressure distributions and streamlines in Figure 5 show the corresponding growth from predominantly attached outer flow to a large recirculating region. The distinction between local wall reversal and the outer streamline pattern is important when interpreting the apparently attached low-angle case.

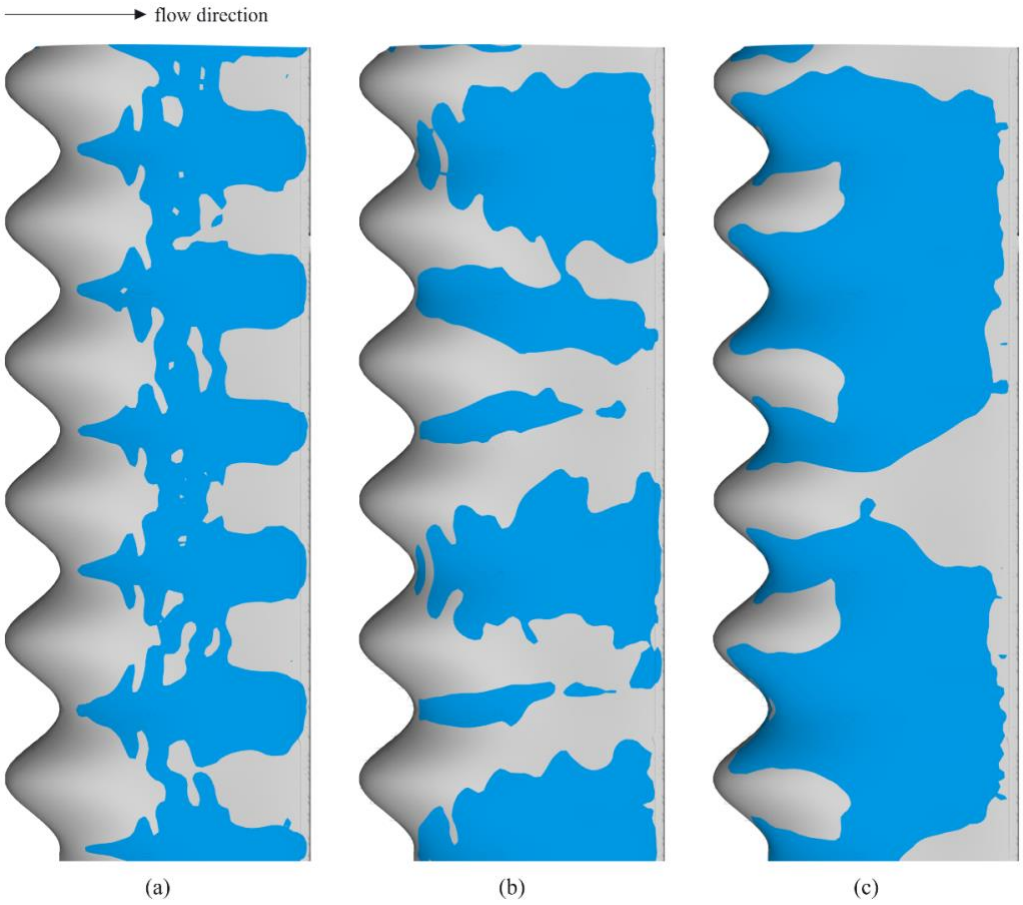


Figure 4. Reversed near-wall flow on the suction side of the reference foil at (a) 5°, (b) 10° and (c) 25°. Blue indicates reversed flow; the incoming flow is from left to right.

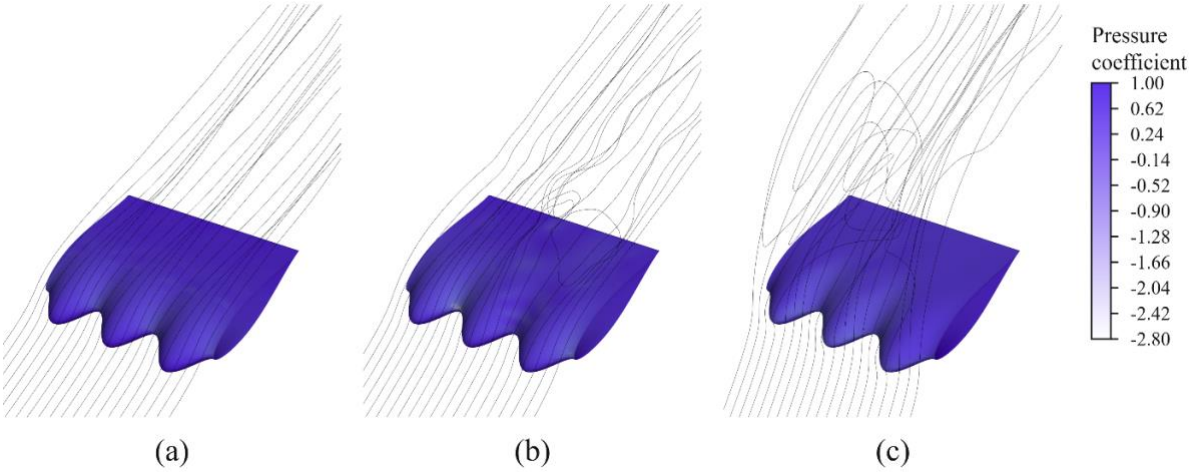


Figure 5. Pressure coefficient and streamlines for the reference foil at (a) 5°, (b) 10° and (c) 25°.

The streamwise-vorticity visualisation shows alternating regions of opposite sign originating near the tubercle shoulders (Figure 6). At 5°, the structures are comparatively ordered and aligned with the streamwise direction. At 10°, they lift away from the surface and interact with the developing separated region; at 25°, they feed a larger separated structure. This is consistent with the local momentum redistribution and cellular separation described in tubercle studies [5,9,10,13]. The observation establishes local counter-rotating structures, but neither their net angular-momentum flux through a downstream propeller disc nor their persistence at the experimental propeller location has been calculated.

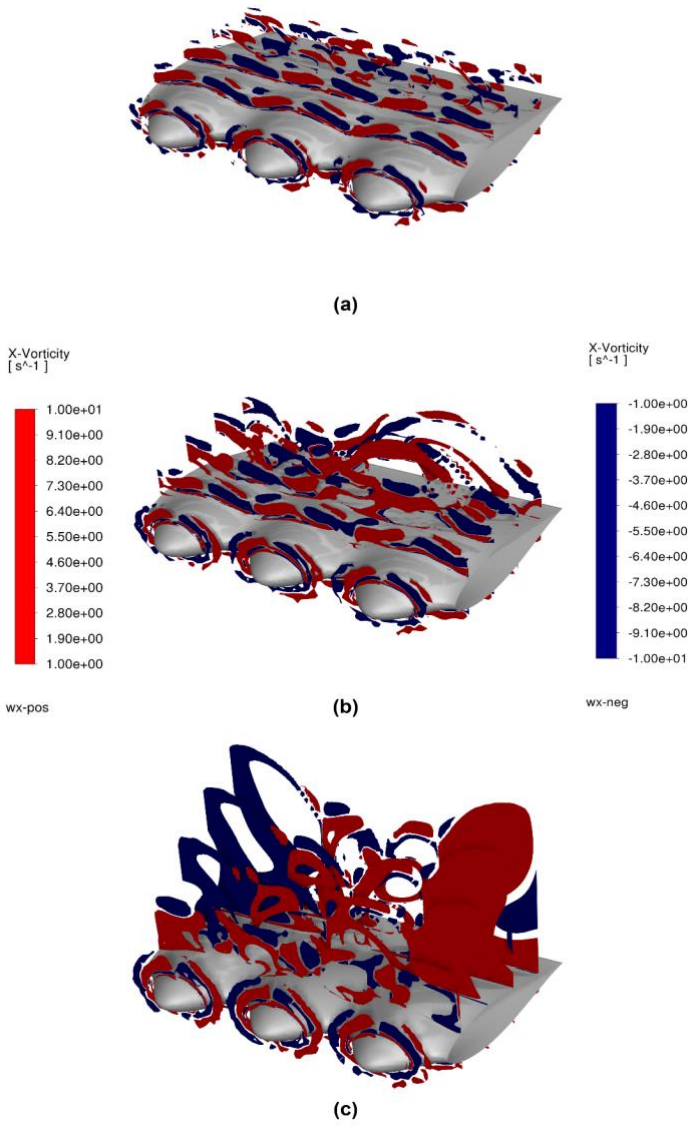


Figure 6. Streamwise-vorticity structures at (a) 5°, (b) 10° and (c) 25°. Red and blue denote opposite signs of streamwise vorticity. These local vortex pairs do not establish a net propeller pre-swirl.

2.4 Pressure fluctuations and the geometric trade-off

The reference foil has a non-monotonic pressure-fluctuation response to incidence (Table 1). Its surface-averaged p′rms rises to 91.7 Pa at 10°, falls to 18.2 Pa at 15°, and subsequently increases overall towards 30°. At 5°, the pressure-fluctuation map contains localised spots near the troughs; at 10°, the distribution becomes less regular and the surface-average reaches its maximum. At 25°, much of the surface has lower fluctuation levels despite extensive mean separation, with isolated elevated regions remaining (Figure 7). The surface maximum and surface average must be distinguished: the reported 25° local maximum is higher than that at 10° (Table 1). Thus, separated area alone does not determine the pressure-fluctuation measure.

Table 1. Reference-foil force and surface pressure-fluctuation results.

α (°)	C_L	C_D	L/D	Mean p′rms (Pa)	Max p′rms (Pa)
0	0.003	0.016	0.16	17.7	227.8
5	0.377	0.039	9.76	40.9	321.6
10	0.488	0.124	3.95	91.7	532.7
15	0.565	0.196	2.88	18.2	154.8
20	0.699	0.290	2.41	41.4	453.1
25	0.799	0.383	2.09	39.2	554.3
30	0.860	0.493	1.75	62.3	359.9

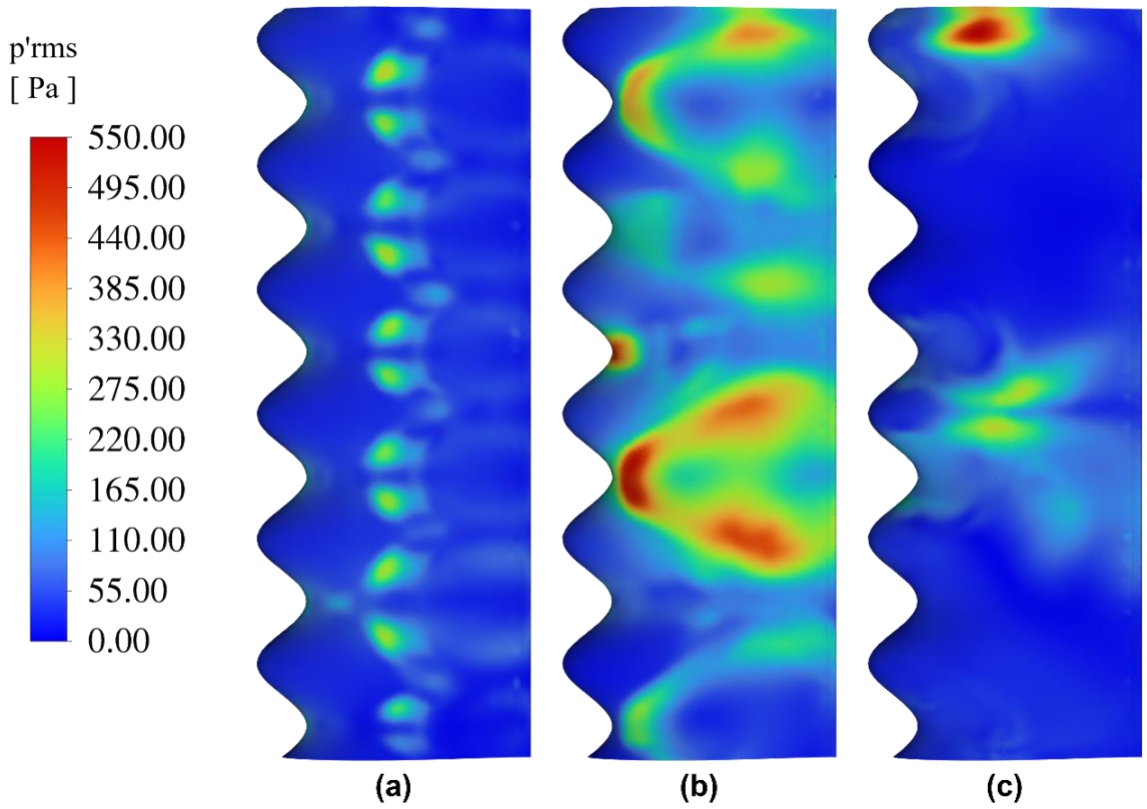


Figure 7. Surface pressure-fluctuation maps for the reference foil at (a) 5°, (b) 10° and (c) 25°, using the same 0–550 Pa colour scale.

Across the 31 tubercled geometries, the arithmetic means over the seven sampled angles show a positive association between L/D and p′rms (Figure 8): Spearman $\rho = 0.70$ with a bootstrap interval of 0.46–0.82. Increasing sinusoidal amplitude generally reduces both quantities in this sampled family. Controlling for amplitude reduces the correlation to 0.25 ($p = 0.19$), consistent with amplitude accounting for much of their association. Wavelength has a secondary influence within the sampled range. The seven-angle average is a campaign summary, not a duty-cycle-weighted ship operating metric. No zero-amplitude foil was included, so these results compare tubercled geometries with one another and cannot establish the benefit of adding tubercles relative to a smooth foil.

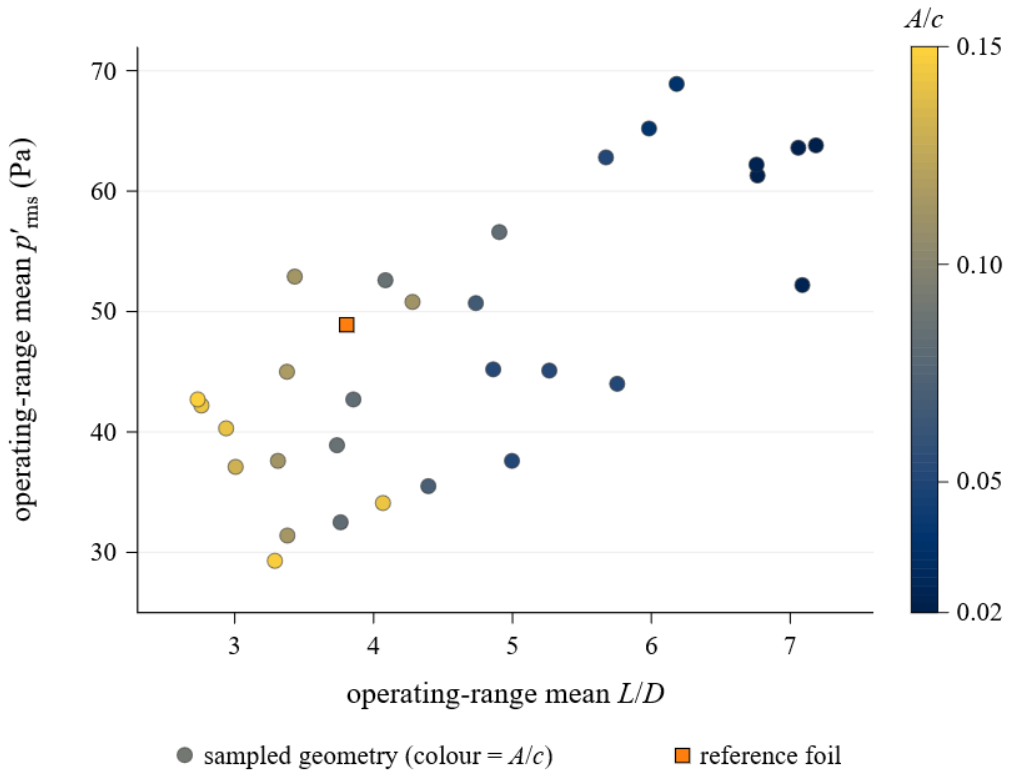


Figure 8. Operating-range mean surface pressure fluctuation versus mean L/D for 31 tubercled geometries. The colour variable A/C in the source figure denotes sinusoidal amplitude and is a/C in this paper.

The numerical evidence therefore identifies a plausible mechanism for a trade-off: geometric changes modify separation and unsteady loading together with the mean forces. It does not show that the geometry with the smallest wall-pressure fluctuation will produce the quietest downstream propulsion system. That distinction motivates the ship-model experiments and the integrated discussion.

3 Experimental investigation on a model ship

The experiments assess the installed hydrofoil–hull–propeller system. They complement the isolated-foil calculations by measuring vessel advance and underwater pressure spectra, but use a different section and much lower Reynolds number. Smooth hydrofoils and a bare-hull condition provide controls for distinguishing installation effects from the incremental effect of tubercles.

3.1 Hydrofoil design

The baseline hydrofoil was based on the NACA 4420 profile. It is thicker than the NACA 4415 profile used in earlier LET studies [9], and the extra thickness provided room for mounting hydrofoils on the

bottom surface of the vessel. Four design parameters were varied (Table 2): the position ahead of the propeller (P), the wingspan (W), the chord length (C) and the number of tubercles (N). Two wingspans (W = 20 and 40 mm) and two chord lengths (C = 20 and 40 mm) were combined, which gave span-to-chord ratios of W/C = 0.5, 1 and 2. These dimensions kept the hydrofoil within the projection of the vessel's outer boundary, so that it was not damaged during docking. Three tubercle numbers were used (N = 0, 5 and 10), where N = 0 denotes a smooth hydrofoil without tubercles, which served as the control for each W–C combination. Figure 2 illustrates the general leading-edge concept; the experimental span and peak-to-trough distance are denoted by W and A, respectively.

The experimental peak-to-trough distance A was fixed at 3 mm, giving A/C = 0.15 at C = 20 mm and 0.075 at C = 40 mm. This convention differs from the numerical sinusoidal amplitude a in Section 2: the corresponding half peak-to-trough distance is A/2 = 1.5 mm, giving (A/2)/C = 0.075 and 0.0375, respectively. For N > 0, the evenly spaced tubercles have λ = W/N, and A/λ = 3N/W takes values 0.375, 0.75 or 1.5. These ratios are twice those obtained with a half peak-to-trough amplitude. The conversion harmonises amplitude definitions only; it does not make the two foil constructions geometrically identical.

The tubercled hydrofoil was built from two profiles: the original NACA 4420 profile, used as the trough profile, and a modified peak profile. Following the peak-and-original-section construction of Fan et al. [9], the peak profile was obtained by shifting the points of the original profile forward with a smooth chordwise function of equation (1).

$$X_{mod}(x) = X_0(x) - \frac{A}{2}\left[1 + cos\left(\frac{\pi X_0(x)}{0.3C}\right)\right] \quad 0 \le X_0(x) \le 0.3C \qquad \textbf{(1)}$$

where X_0 is the chordwise coordinate of a point on the original profile, measured from the leading edge (X_0= 0) towards the trailing edge (X_0 = C), X_{mod} is the coordinate of the same point on the peak profile, A is the amplitude and C is the chord length of the original profile. Points behind X_0 = 0.3C were not shifted. The shift equals A at the leading edge, so the peak profile has a chord of C + A. The shift and its slope both vanish at X_0 = 0.3C, the position of maximum thickness, so the modified region blends smoothly into the unchanged aft section. The peak and trough profiles were placed alternately at intervals of λ/2 along the span, with a trough section at each end, and joined with the "Loft" function of the CAD software to form a smooth leading-edge waveform with N peaks. The hydrofoils were manufactured by 3D printing in PLA.

The four factors define a full factorial of 3 × 2 × 2 × 3 = 36 combinations. Thirty were tested, numbered C2–C31 (Table 2), together with a reference without a hydrofoil (C1). The six omitted combinations were the 20 mm × 20 mm hydrofoils with 5 and 10 tubercles at each position. The design is therefore incomplete: smooth hydrofoils were tested at all four span–chord combinations, whereas N = 5 and 10 were tested at three. Statistical interpretation of this imbalance is addressed in Section 3.3.3.

Table 2. The parameters detail for each hydrofoil testing case. C1 is the reference case without a hydrofoil. N = 0 denotes a smooth hydrofoil

Label	Position (mm)	Wingspan (mm)	Chord length (mm)	Number of tubercles
C1	None	None	None	None
C2	30	40	40	0
C3	100	40	40	0
C4	170	40	40	0
C5	30	40	40	5
C6	100	40	40	5
C7	170	40	40	5
C8	30	40	40	10
C9	100	40	40	10
C10	170	40	40	10
C11	30	40	20	0
C12	100	40	20	0
C13	170	40	20	0
C14	30	40	20	5
C15	100	40	20	5
C16	170	40	20	5
C17	30	40	20	10
C18	100	40	20	10
C19	170	40	20	10
C20	30	20	40	0
C21	100	20	40	0
C22	170	20	40	0
C23	30	20	40	5
C24	100	20	40	5

C25	170	20	40	5
C26	30	20	40	10
C27	100	20	40	10
C28	170	20	40	10
C29	30	20	20	0
C30	100	20	20	0
C31	170	20	20	0

3.2 Experimental setup

3.2.1 Towing tank and model vessel

The experiments were performed in a towing tank 30 m long and 1.9 m wide, with a water depth of 1.5 m (Figure 9). The 7.5 m testing area was located at the tank centre. Two stereo cameras were mounted 1.7 m above the water level to measure vessel velocity (Section 3.3.2). Wooden frames formed a rail system that constrained the aluminium mast and guided the vessel along a straight path. The PLA hull was 3D-printed at a length scale of 1:191 and was similar to the KVLCC2 tanker hull used in earlier experimental and CFD studies [33]. Model and full-scale particulars are listed in Table 3 [34,35]. The nominal test velocity was U = 0.216 m/s, giving Fr = 0.0533. The hydrofoils were mounted 30, 100 or 170 mm ahead of the propeller blade section.

Table 3. Particulars of the model vessel and KVLCC2 tanker [34,35]

	Model	KVLCC2
Length of Hull (m)	1.675	320.0
Maximum Breadth (m)	0.3036	58.0
Depth (m)	0.157	30.0
Draught (m)	0.109	20.8
Test Velocity (m/s)	0.216	2.986
Froude Number	0.0533	0.0533

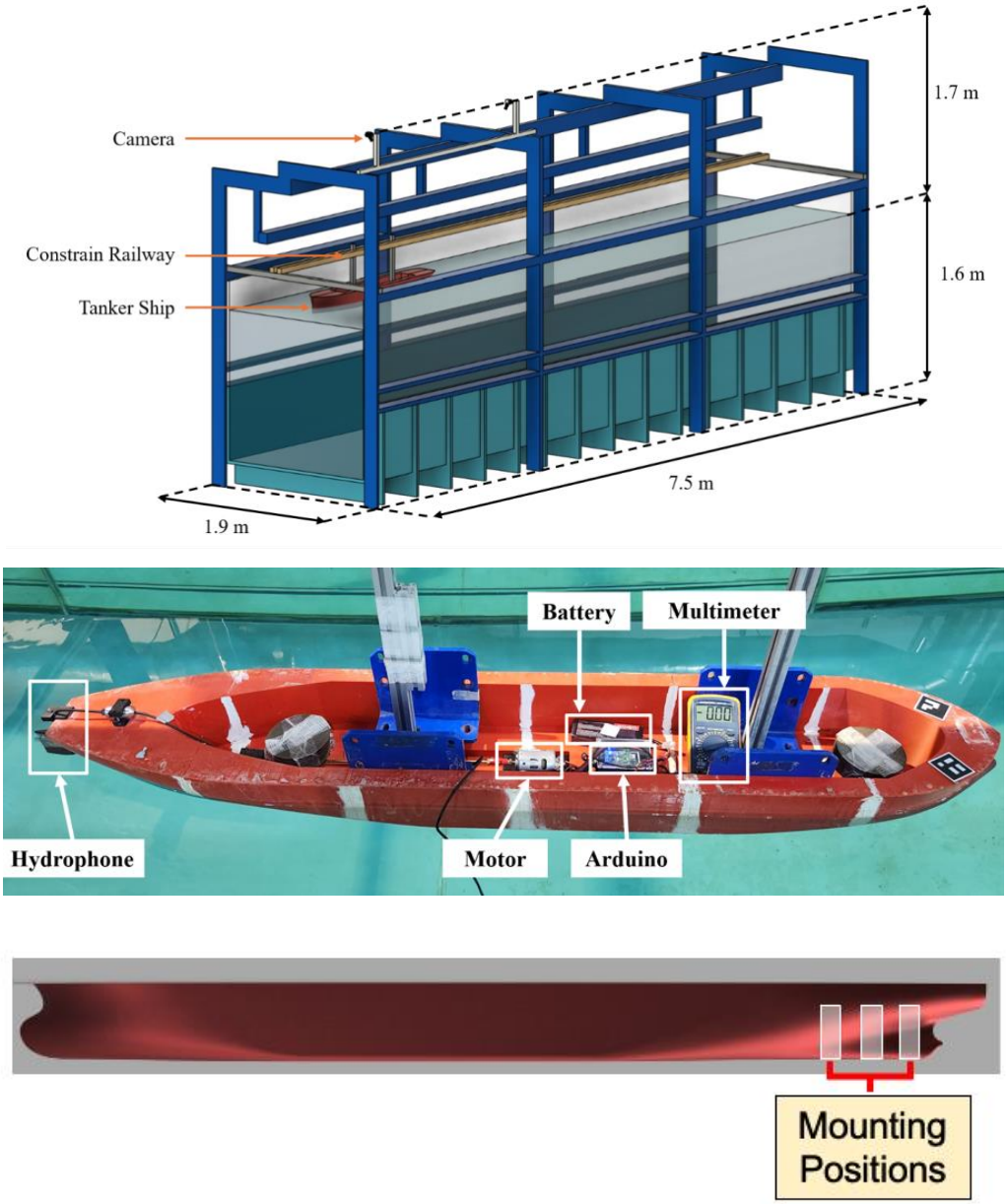


Figure 9. The towing tank (top) and the testing model vessel (bottom)

3.2.2 Test series

Five repeated tests were planned for each hydrofoil configuration, with four or five retained per configuration and 147 hydrofoil runs in total. The configurations were tested in the order in Table 2. Approximately one minute was allowed between runs for the water surface to settle; water temperature was not measured. The motor battery was recharged or replaced after each nine configurations. DPR was used to express advance per revolution and reduce dependence on absolute rotational speed, but

this ratio does not guarantee independence from changes in the operating point and is not a measure of propulsion power or efficiency (Section 3.3.2).

a) The underwater background noise was first quantified for the testing environment to determine its significance. All devices remained turned off while the ship was stationary. The background noise was considered negligible if it is more than 10 dB below the noise level recorded during subsequent testing.
b) Blade-generated noise was isolated from mechanical and electrical vibration by comparing two propeller conditions: a blade-less dummy propeller and a regular propeller, both rotated at a matched speed of approximately 9.25–11.4 revolutions per second while the vessel remained stationary. This procedure followed ITTC guidance [22].
c) A reference dynamic test provided baseline noise and velocity data for comparison with the hydrofoil results. The vessel travelled freely along the towing rail without a hydrofoil installed, using the same regular propeller described above.
d) Finally, all 30 hydrofoil configurations listed in Table 2 were tested dynamically under the same conditions as the reference case, with the hydrofoil mounted upstream of the propeller at the position, wingspan, chord length, and tubercle number specified for each configuration.

3.3 Data processing and statistical analysis

3.3.1 Pressure spectra

Underwater pressure was measured using an Aquarian Scientific AS-1 hydrophone connected to an AMS-22 amplifier. The hydrophone was located 35 mm downstream of the propeller centre (Figure 10), and the signal was sampled at 44.1 kHz. At this close location, the recording may contain hydrodynamic pressure fluctuations as well as acoustic pressure. The reported spectra are therefore local underwater pressure measurements rather than a separated far-field radiated-noise metric.

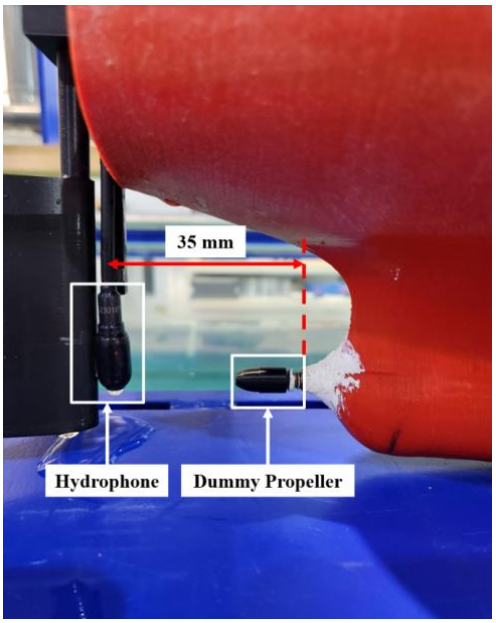


Figure 10. The hydrophone position demonstrated using a no-blade dummy propeller

The average power spectral density $G(f)$, in units of μPa²/Hz, was estimated from each sound pressure signal using Welch's method with Hann window. The resulting sound pressure spectral density level (L_p) is calculated as:

$$L_p = 10\, log_{10}\left(\frac{G(f)}{{p_{ref}}^2}\right) \quad \textbf{(2)}$$

where p_{ref} = 1 μPa and L_p is in unit of dB re 1μPa²/Hz [21,22].

Prior to computing the final L_p spectrum, the raw signal was processed using a Short-Time Fourier Transform (STFT) to check for interference, as shown in Figure 11. The resulting spectrogram was visually inspected to identify interference-free segments initially; a sudden colour change indicated an abrupt shift in the noise signature. Data recorded beyond this point were therefore excluded from analysis. All data were processed within a minimum 20 second window where the ship speed is stable, following ITTC guidance [21,22] . The position of this window was selected among the four or five repeat measurements of each configuration. The target frequencies were identified by the spectrum peak after Fourier transform. Throughout data collection, the recorded voltage remained within the amplifier's full-scale range, confirming that no signal clipping or distortion occurred.

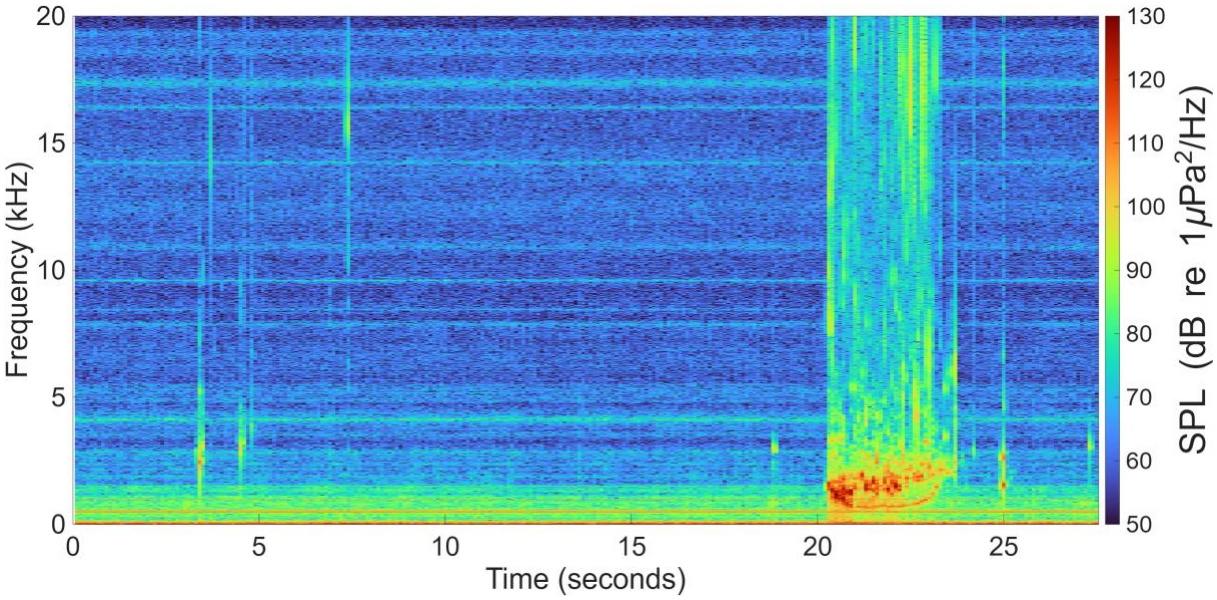


Figure 11. The Short-Time Fourier Transform

3.3.2 Velocity and distance per revolution

Two identical cameras (DAHeng Imaging MER3-1610-52U3DM) with frame of 20 fps, were mounted 1.7 m above the towing tank, approximately 2 meters apart, with their fields of view overlapping to cover the 1 m test section.

Three position markers (P1, P2, P3) were placed at equal intervals of 0.5 m over the 1 m terminal test section, representing the start, mid-way and end points respectively (Figure 12). As the vessel passed each marker, the corresponding stereo image pair was recorded together with its frame number and timestamp. The vessel velocity over each half-section (P1–P2 and P2–P3) was calculated as the marker spacing divided by the elapsed time between the corresponding frames, and the two half-section velocities were compared to verify that the vessel had reached a steady speed within the test section. The mean of the two segment velocities was then used as the representative vessel velocity for each run.

The vessel's motor was powered by a 7.4 V lithium battery under 1 V. The voltage output of which dropped with continued use, reducing the propeller rotational speed and vessel speed. Because this drop affected the motor and the resulting thrust in a broadly proportional manner, the ratio between vessel speed and propeller rotational speed, which is the distance per revolution (DPR, equation (3)), was expected to remain largely insensitive to this effect. The propeller rotational speed was determined by the corresponding frequency of the maximum L_p peak, and DPR was therefore used, alongside the camera-derived velocity, to characterise vessel performance.

$$DPR = \frac{U}{RPS} \quad \textbf{(3)}$$

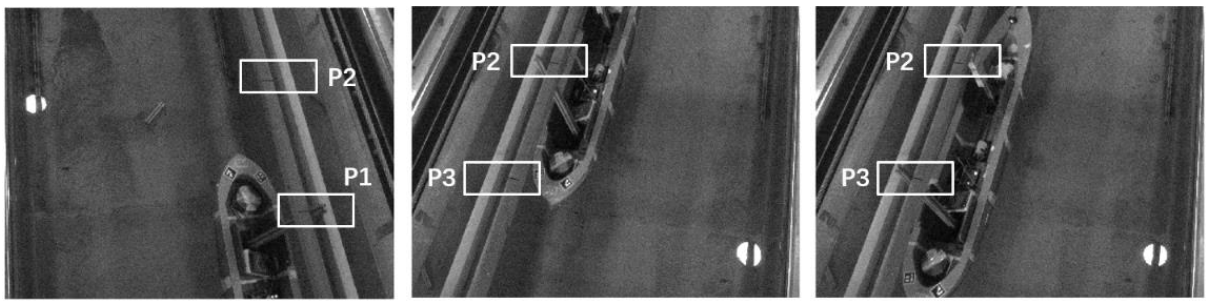


Figure 12. Stereo camera image capturing vessel movement, with position markers P1, P2, and P3 highlighted

3.3.3 Statistical analysis

The retained experimental measurements were analysed using coefficients of variation (CV), one-way analysis of variance (ANOVA), and residual-based net-effect comparisons. CV characterised repeatability within configurations. ANOVA and net-effect comparisons used the 30 hydrofoil configuration means, so repeated runs were not treated as independent design points.

CV was calculated using equation (4), where μ and σ are the mean and standard deviation of repeated measurements. It is used for positive linear quantities such as velocity, RPS and DPR. Repeatability of the logarithmic pressure spectral level Lp is expressed using its standard deviation in dB.

$$CV = \frac{\sigma}{\mu} \tag{4}$$

One-way ANOVA was applied separately to mounting position P, wingspan W, chord length C and tubercle number N. Equations (5)–(8) define the between-group and within-group sums of squares, their mean-square ratio F and the corresponding p-value. Here k is the number of factor levels, n is the number of configuration means, and g indexes groups. A p-value below 0.05 was treated as an exploratory indication of a factor-associated difference. Because the design is incomplete, these one-factor tests do not isolate interactions or establish causation. Response frequencies at which at least one parameter was significant were carried forward to the residual-based comparisons.

$$SS_{between} = \sum_{g=1}^{k} n_g \left(\bar{y}_g - \bar{y}\right)^2 \tag{5}$$

$$SS_{within} = \sum_{g=1}^{k} \sum_{i=1}^{n_g} \left(y_{gi} - \bar{y}_g\right)^2 \tag{6}$$

$$F = \frac{SS_{between}/(k-1)}{SS_{within}/(n-k)} \tag{7}$$

$$p = P\left(F_{k-1,n-k} \geq F\right) \quad \textbf{(8)}$$

A net effect analysis was used to quantify the direction and magnitude of the change in the response caused by each parameter after the influence of the other three parameters had been removed.

For a target parameter d, the response of the 30-configuration means was first regressed by ordinary least squares on the other three parameters, each treated as a categorical variable using equation (9) [36]. y_i is the response (the L_p in dB or the DPR in mm/rev) of configuration i, $\mathcal{C}$ is the set of the other three parameters, $\mathbb{1}[x_{i,j}]$ are the indicator (dummy) variables for the levels of parameter j (excluding its reference level), β_0 is the intercept, β_j are the regression coefficients, and e_i is the residual, which contains the effect of d together with random error.

$$y_i = \beta_0 + \sum_{j \in \mathcal{C}} \beta_j \ \mathbb{1}[x_{i,j}] + e_i \quad \textbf{(9)}$$

The net effect of level ℓ of parameter d was defined as the mean residual of the configurations at that level using equation (10). n_ℓ is the number of configurations at level ℓ. A positive (negative) $\bar{e}_\ell$ means that the response at this level was higher (lower) than expected from the other three parameters, and the difference between two levels gives the size of the effect of changing d, in the unit of the response. The difference between two levels ℓ_a and ℓ_b was tested with a two-sample t-test on the residuals, using equation (11), and $p < 0.05$ was taken as significant.

where $s^2{}_\ell$ is the sample variance of the residuals at level ℓ. The parameters with two levels (W and C) gave one comparison each, and those with three levels (P and N) gave three.

$$\bar{e}_\ell = \frac{1}{n_\ell} \sum_{i:\, d_i = \ell} e_i \quad \textbf{(10)}$$

$$t = \frac{\bar{e}_{\ell_b} - \bar{e}_{\ell_a}}{\sqrt{s^2_{\ell_a}/n_{\ell_a} + s^2_{\ell_b}/n_{\ell_b}}} \quad \textbf{(11)}$$

The analysis was applied to the seven target frequencies at which the ANOVA found at least one significant parameter, and to all four parameters at each of them, which gave 56 comparisons. Net effect analysis adjusts for the other parameters assuming that their effects are additive, so interactions between parameters could not be assessed. Because the design is unbalanced, the residual-based estimate is slightly smaller in magnitude than the coefficient of a model containing all four parameters, so it is conservative. The comparisons were not corrected for multiple testing; at the 0.05 level about 2.8 (56 × 0.05) significant results are expected by chance, which is considered in the interpretation (Section 3.4).

3.4 Experimental results

3.4.1 Noise sources and target frequencies

The L_p spectra from 0 to 50 Hz of the four baseline conditions are compared in Figure 13, computed with 2000 ms windows, a frequency resolution of 0.5 Hz. The background spectrum is nearly flat, between 75 and 85 dB re 1 μPa²/Hz. With the motor powering a no-blade propeller (NoBlade), the spectrum peaks appear at approximately 13, 26.5 and 39.5 Hz, corresponding to the shaft rotation frequency and its second and third harmonics. These peaks reach about 120 dB, while the broadband level between them remains close to the background. With the regular three-blade propeller fitted in the static test (RegularSt), the same series appears at approximately 10.5, 21 and 31.5 Hz. As the voltage input was the same, the lower shaft frequency is probably caused by the additional hydrodynamic load of the propeller. For this three-bladed propeller, the blade-passing frequency (3 × 10.5 Hz ≈ 31.5 Hz) coincides with the third shaft harmonic. The dynamic test (RegularDy) shows the same harmonic series, with the whole spectrum 5 to 12 dB higher. Possible causes are effects that are present only when the vessel is moving, such as non-uniform inflow from the hull wake and hydrodynamic pressure fluctuations, but the present data cannot separate their contributions.

The peak near 21 Hz requires particular care. The observations are as follows. In RegularSt, the peak at 21 Hz coincides with the second harmonic of the 10.5 Hz shaft frequency (2 × 10.5 = 21 Hz). However, the NoBlade spectrum also contains a tonal peak at about 21 Hz (about 119 dB), which is not a harmonic of its own 13 Hz shaft frequency, since the second harmonic of 13 Hz is the 26.5 Hz peak. The STFT shows that this component is present throughout the NoBlade recording, as persistently as the 13 Hz component. In the additional static tests at 1800 and 4300 mV, the motor rotated faster, giving shaft frequencies of approximately 15 and 19.5 Hz and spectrum levels 20–23 dB higher than the regular static test at 1000 mV, and no peak appears at 21 Hz (Figure 13). A fixed-frequency source would remain at 21 Hz regardless of rotation speed, so the absence of the peak at higher voltages suggests that the 21 Hz peak in RegularSt is the second shaft harmonic rather than a fixed-frequency motor tone. This is not conclusive: a weak fixed tone could be masked by the higher broadband level at these voltages, and in RegularSt a shaft harmonic and a fixed tone would fall at the same frequency and cannot be separated. The origin of the 21 Hz tone in the NoBlade condition remains unresolved.

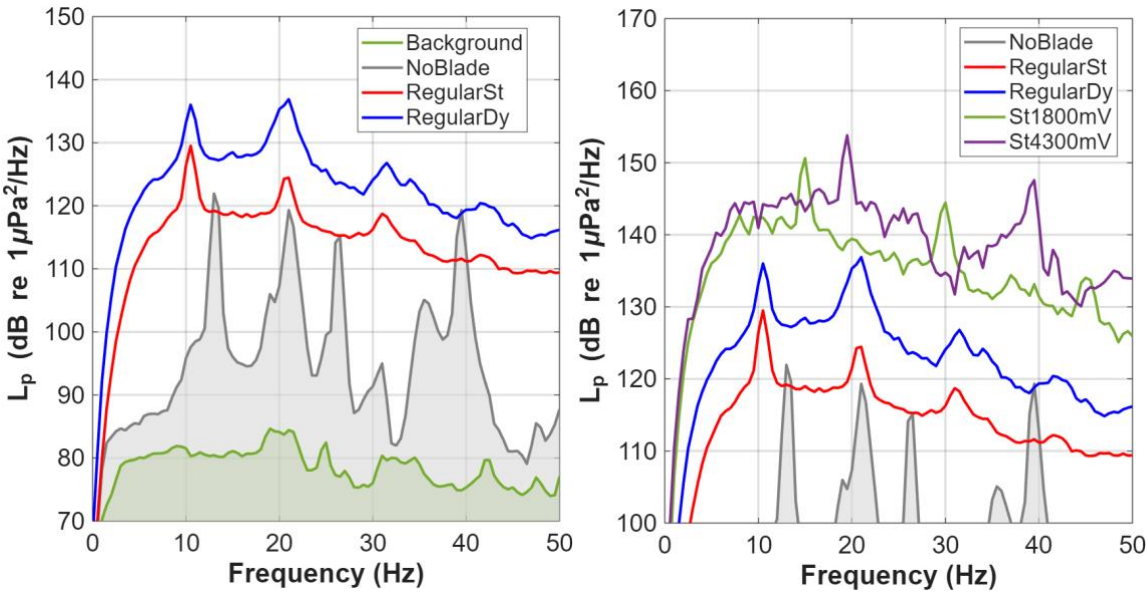


Figure 13. The $\boldsymbol{L_p}$ for shaft and propeller frequencies at baseline conditions (left)and static test with greater voltage input (right)

The result of L_p at higher frequency is shown in Figure 14, using 50 ms windows and frequency resolution of 20 Hz. Background noise was at least 12 dB lower than all other conditions, confirming it did not confound the results. In both the static and dynamic tests, spectral peaks appear at 500, 1000, 4120, 7880, 8440, 9580, 10860, 14200, 16420, 17360, 18580 and 19340 Hz. These frequencies were selected as the target frequencies for the hydrofoil analysis because first, they are narrow-band components that stand out above the broadband spectrum; and second, they were present in both the static and the dynamic tests, the latter being the condition of the hydrofoil tests; and last, they cover the range from 500 to 19340 Hz. The 20 Hz band was added because, with the 20 Hz resolution, it contains the shaft frequency and its second harmonic. When the voltage input was increased to 1800 and 4300 mV (Figure 15), the target frequencies did not shift. They are therefore not harmonics of the shaft rotation.

Particular attention was paid to 500 and 19340 Hz, where peaks of similar width appear in both the NoBlade and the regular-propeller conditions, showing in Figure 15, so these peaks are not generated by the blades. The 500 Hz peak is absent from the background recording, which indicates that it comes from the powered motor or other equipment; this could be tested by measuring at the minimum voltage before the motor starts rotating. The 19340 Hz peak is close to the Nyquist frequency of the recording, 22.05 kHz for a 44.1 kHz sampling rate, so it may be an artefact, which could be checked with a higher sampling rate such as 96 kHz. The L_p at 20, 500 and 19340 Hz is therefore interpreted with caution in the analysis of the hydrofoil effects.

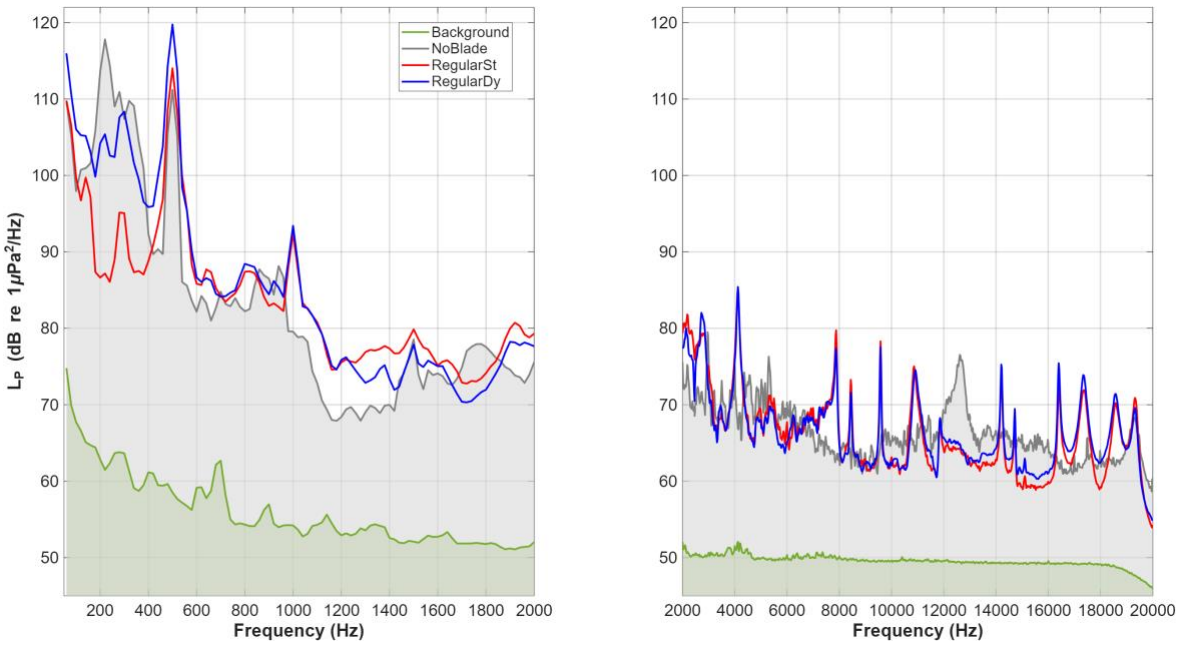


Figure 14. The L_p for different test series between 50 Hz and 20000 Hz

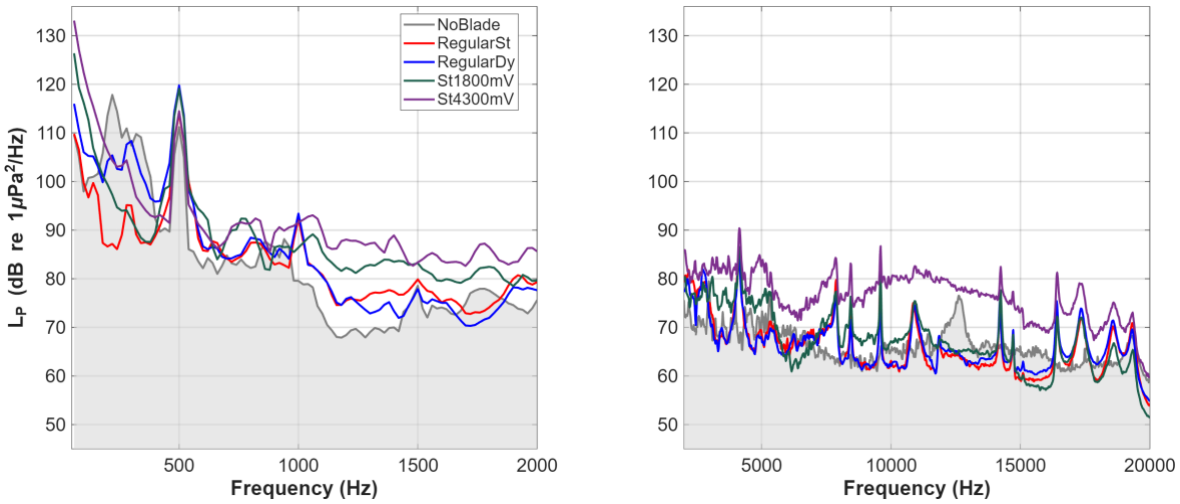


Figure 15. The L_p with greater voltage input

3.4.2 Hydrofoil and bare-hull performance

Experiments were performed with the 30 hydrofoil configurations and the bare hull reference conditions. The L_p and DPR of each run are plotted in Figure 16, and the CV of the four or five repeats of each hydrofoil configuration is shown in Figure 17.

The comparison reference was the bare hull tested on different days. The bare hull results varied between runs. The DPR averaged 20.44 mm/rev with SD = 1.08 mm/rev. 73.3% fell within ±1.0 mm/rev. For L_p, averaged over the 13 frequency bands, 80% of the runs fell within ±2 dB and 94.4% within ±3 dB of the mean, although the share at ±3 dB varied from 80–86.7% at 4120, 7880 and 10860 Hz to 100% at 9580, 14200 and 18580 Hz. When both criteria were applied together, 71.8% of the bare hull runs lay inside a window of ±3 dB and ±1.5 mm/rev. The causes of the variation were not identified; possible causes are changes in the vessel launching conditions, the water temperature and residual water motion in the tank.

Across the 30 hydrofoil configurations with a total of 147 runs, the mean velocity was 220.9 mm/s, the mean RPS was 10.69 Hz and the mean DPR was 20.67 mm/rev, which were close to the bare hull values of 216.09 mm/s, 10.56 Hz and 20.44 mm/rev. The configuration-mean DPR ranged from 18.40 to 22.03 mm/rev, corresponding to a deviation of −2.04 to +1.59 mm/rev from the bare hull mean. Nine of the 30 hydrofoils exceeded the bare hull DPR by more than 1 mm/rev, 17 fell within ±1 mm/rev, and the other 4 were lower by more than 1 mm/rev.

For L_p, the configuration-mean level averaged over the 13 bands was 0.71 dB higher than the bare hull and ranged from −1.07 to +3.17 dB, and 13 of the 30 configurations were more than 1 dB higher. The offset depended on the frequency. It was largest at 14200 Hz at +3.19 dB, 16420 Hz at +2.30 dB and 17360 Hz at +2.02 dB, whereas the levels at 4120 Hz, 20 Hz and 500 Hz were slightly lower than those of the bare hull, by 0.57, 0.27 and 0.23 dB, respectively. On average, 83.3% of the band-level differences between a configuration and the bare hull were within ±3 dB, and only three configurations had all 13 bands within ±3 dB. The levels exceeded the bare hull by more than 3 dB for 19 configurations at 14200 Hz, 8 at 17360 Hz, 6 at 16420 Hz and 5 at 1000 Hz. Levels fell more than 3 dB below the bare hull for 11 band–configuration combinations, at 20, 500, 1000, 10860 and 19340 Hz, with the lowest difference of −7.03 dB.

No configuration was clearly quieter than the bare hull. The lowest mean offset was −1.07 dB for P100W40C40N0, which was smaller than the bare hull SD of 1.71 dB. The three quietest configurations were P100W40C40N0 at −1.07 dB, P30W40C20N5 at −0.83 dB and P170W40C40N0 at −0.73 dB. They were lower than the bare hull in 9, 8 and 8 of the 13 bands, respectively, and all had W = 40 mm. Among them, P170W40C40N0, a smooth hydrofoil, also had a high DPR of 21.98 mm/rev, which was 1.54 mm/rev above the bare hull. It was the only configuration with a lower L_p, and a DPR increase of more than 1 mm/rev, so it was the best compromise between noise and DPR. The effect of tubercles

depended on the chord length. For W = 40 mm and C = 20 mm, tubercles lowered the mean L_p, offset from +1.30 dB without tubercles to −0.55 dB with N = 5 and −0.16 dB with N = 10, whereas for C = 40 mm they raised it from −0.53 dB without tubercles to +0.64 dB with N = 5 and +2.59 dB with N = 10. For W = 20 mm and C = 40 mm, tubercles had little effect, with offsets of +1.01, +1.04 and +1.11 dB for N = 0, 5 and 10. The four loudest configurations had offsets of +2.17 to +3.17 dB, and all had W = 40 mm, C = 40 mm and N = 5 or 10. Their largest excess was at 16420 Hz at +5.2 dB, 14200 Hz at +4.8 dB and 17360 Hz at +4.0 dB. The quieter tubercled configurations also had a lower DPR. W40C20N5 had a mean DPR of 19.32 mm/rev, which was 1.12 mm/rev below the bare hull. This indicates a trade-off between noise and DPR, similar to the noise–efficiency trade-off of propellers reported by Knox et al. [19]. The influence of each design parameter is analysed in Section 3.4.3.

The within-configuration repeatability was high. The median CV of the hydrofoil configurations was 2.91% for velocity, 1.4% for RPS and 2.36% for DPR. The maxima were 10.49% for velocity and 3.70% for RPS, both for P170W20C20N0, and 9.18% for DPR, for P170W40C20N5. The CV of the 15 bare hull runs was 7.24% for velocity, 2.55% for RPS and 5.28% for DPR. A velocity CV below 2.46% was found for 13 configurations and a DPR CV below 2.46% for 16. The within-configuration standard deviation of L_p averaged 0.60 dB, with a median of 0.52 dB, compared with 1.71 dB among the 15 bare hull runs.

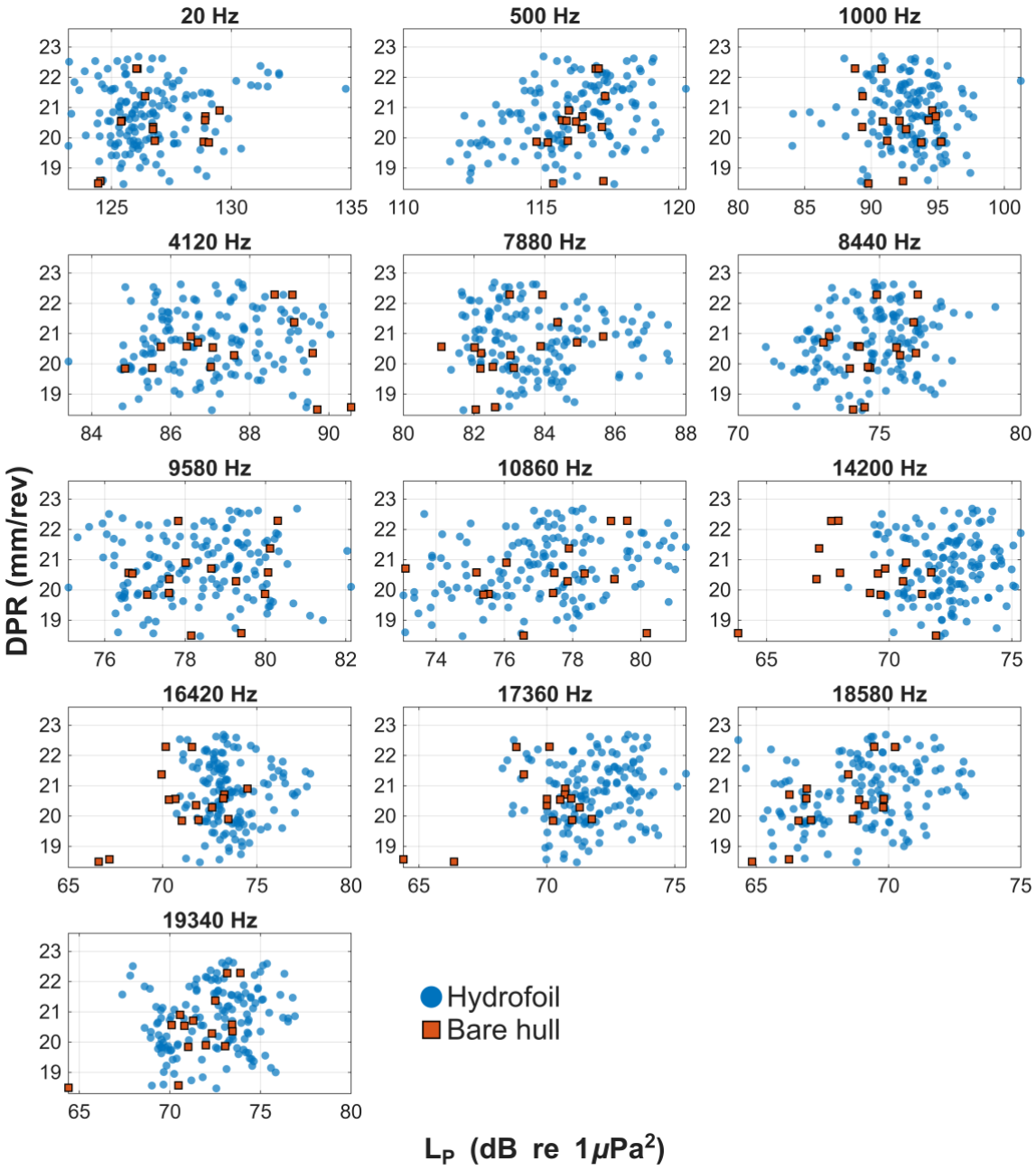


Figure 16. DPR and L_p data for hydrofoil and bare hull conditions at target frequencies.

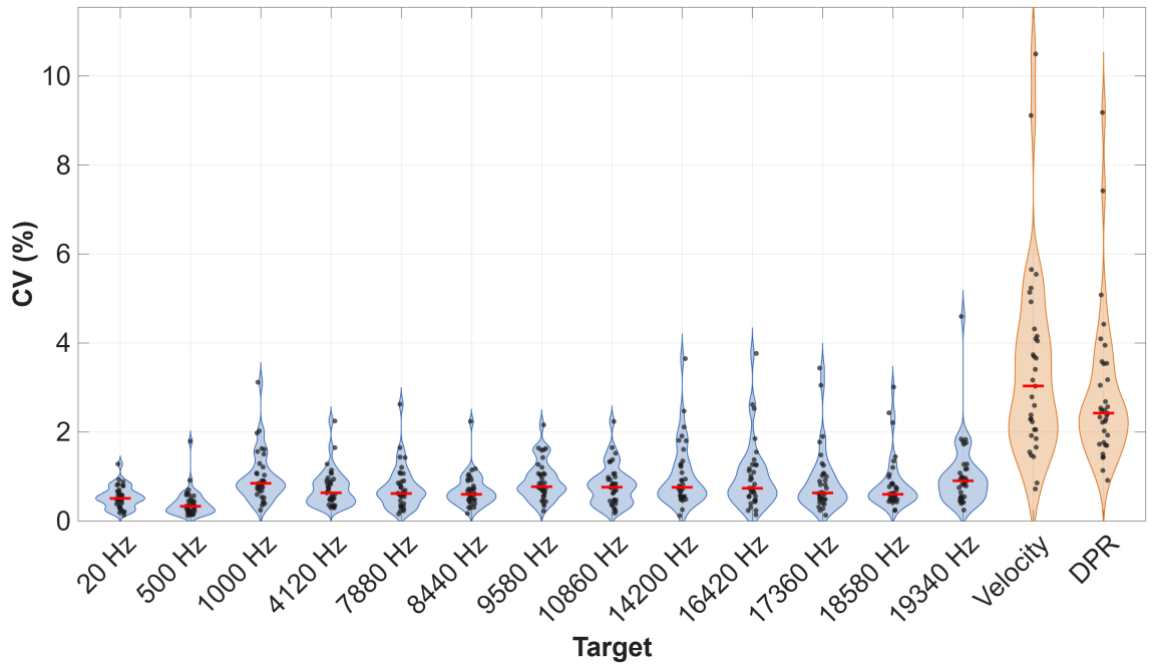


Figure 17. Violin plot with CV in each target parameter

3.4.3 Effects of design parameters

The one-way ANOVA for each design parameter at the 13 target frequencies and for DPR is shown in Figure 18 with its F value. The analysis used the means of the 30 configurations, so that repeated runs of the same configuration were not treated as independent samples. The F value indicates the impact of a parameter: a larger F means that changing the parameter produces a larger difference between levels relative to the variation within levels. The p value indicates the reliability of this difference, and a threshold of 0.05 was applied. Filled markers show $p < 0.05$, where the effect was considered reliable, and hollow markers show $p \geq 0.05$. The critical F value at $p = 0.05$ is 4.20 for W and C, which are two-level targets; and 3.35 for P and N, the three-levels target. All filled markers lie to the right of these values and F values of different parameters cannot be compared directly.

Of the 56 tests, with 4 parameters in 14 targets, 9 were significant, whereas none was significant for P or N. No parameter reached significance at L_p targets for 20, 1000, 8440, 10860, 16420 and 17360 Hz or for DPR. The rest seven L_p frequencies had at least one significant parameter. W is significant in five targets, including 500, 7880, 9580, 18580 and 19340 Hz. It is maximum at 9580 Hz with F = 11.98. C is showed in four of 500, 4120, 9580 and 14200 Hz, maximum at 14200 Hz with F = 16.02. Notice in 500 Hz, both W and C were only marginally significant with F = 4.39 and p = 0.045.

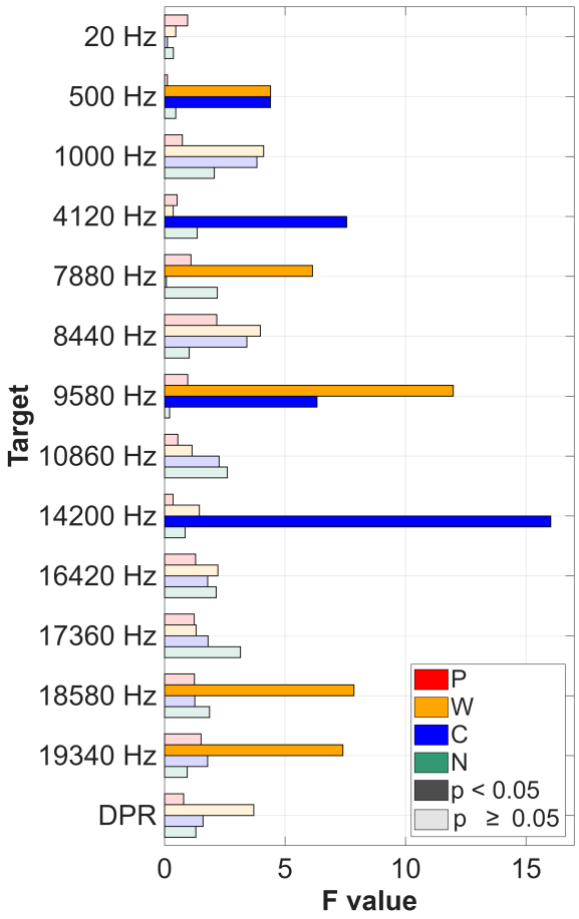


Figure 18. The ANOVA result on target frequencies and DPR with the four design parameters: P (position), W (wingspan), C (chord length), N (number of tubercles).

While the ANOVA measure the importance of the changes in design parameters, the net effect indicates their direction. For the seven frequencies target which showed significant in the ANOVA, they were carried into the net effect analysis, with their result displayed in Figure 19. It shows the net effect of each parameter after the other three parameters were removed. Each marker is the mean residual of one level, in dB, and the stars above the panels mark the pairwise differences between levels that were significant in a two-sample t-test with equal variances. "*" indicates the p value in t-test is less than 0.05, where "**" and "***" resulting in $p < 0.01$ and $p < 0.001$. Of the 56 pairwise comparisons, 11 were significant: 5 of 7 for W, 3 of 7 for C, 3 of 21 for N and 0 of 21 for P. P therefore showed no significant net effect at any frequency, which agrees with the ANOVA.

The direction of the effects depended on the parameter and the frequency. Increasing the chord length C from 20 to 40 mm raised L_p at all three significant frequencies, 1.54 dB at 4120 Hz, 1.32 dB at 14200 Hz and 0.76 dB at 9580 Hz. Increasing the wingspan from 20 to 40 mm lowered L_p at the three highest frequencies, which are 1.09 dB at 9580 Hz, 1.67 dB at 18580 Hz and 1.79 dB at 19340 Hz, but raised it at the two lower frequencies, as 0.85 dB at 4120 Hz and 1.03 dB at 7880 Hz. The effect of N was not

monotonic. At 4120 Hz, the net effect of N = 0 was +0.7 dB and both N = 5 and N = 10 were lower by 1.26 dB and 1.09 dB, with no difference between N = 5 and N = 10. At 18580 Hz, N = 10 was 1.74 dB louder than N = 5 (p = 0.024), and N = 0 lay in between. N had no significant effect at 7880, 9580 or 14200 Hz.

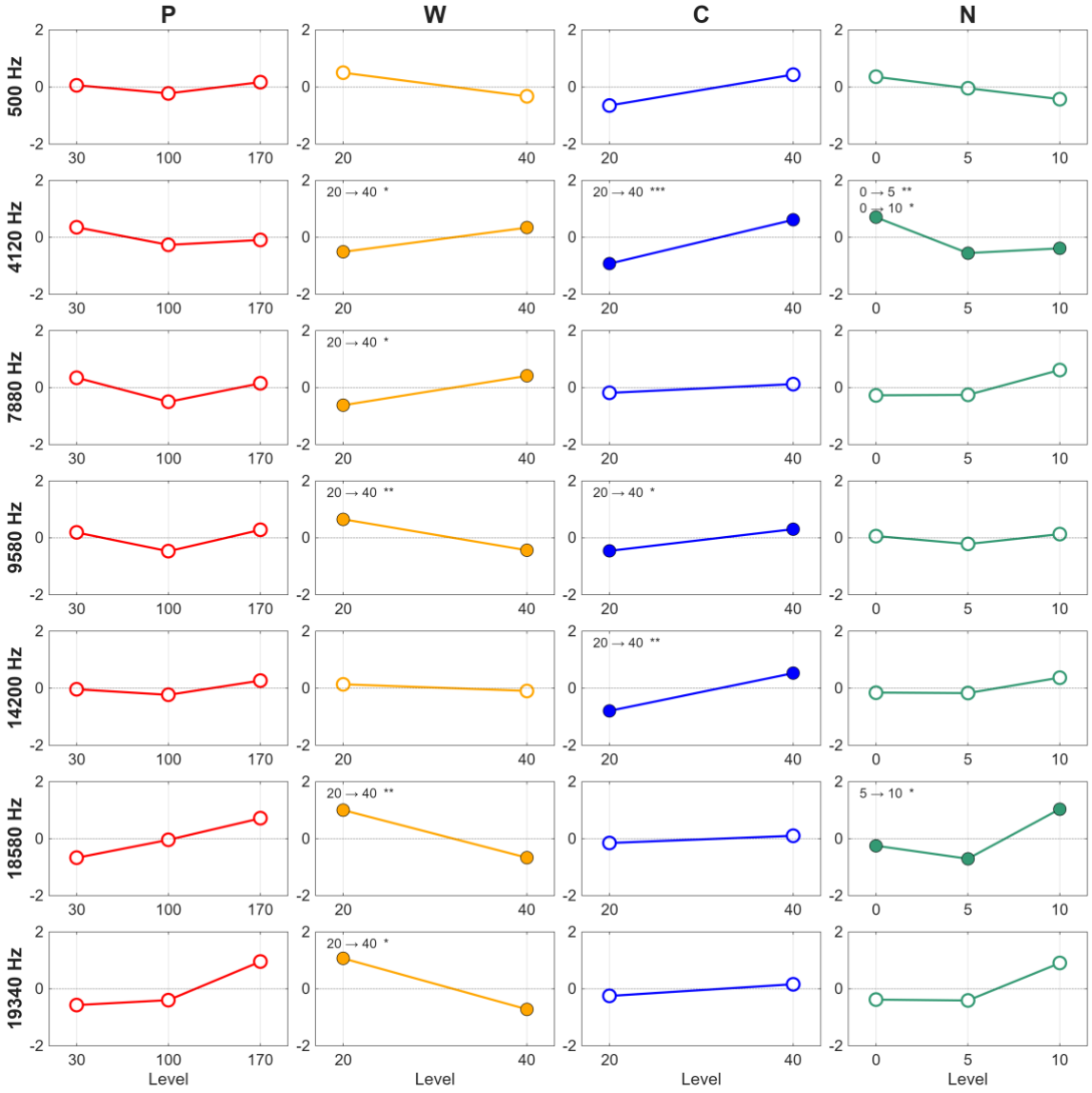


Figure 19. The net effect of the design parameters in dominant target frequencies

4 Integrated discussion of flow mechanisms and system response

4.1 Hull-wake vortices and hydrofoil-mediated flow control

As water passes along the hull and into the aft body, the growing boundary layer, hull curvature and adverse pressure gradient produce a non-uniform wake containing coherent vortical structures. Full-scale analyses identify bilge and side vortices, their interaction and their influence on the velocity deficit

approaching the propeller [37,38]. These structures develop along the hull and aft body rather than originating at a single universal midship location. A propeller operating in this wake experiences spatially and temporally varying inflow, which changes blade incidence and loading. The resulting load fluctuations can promote vibration and, where cavitation occurs, cavitation-related noise [20,38]. Wake losses and propeller–wake interaction can affect the power required for propulsion, but their net contribution cannot be inferred from vortex strength alone.

The proposed role of the upstream hydrofoil is to interfere with these hull-generated structures before they reach the propeller. Its streamwise vortex pairs and induced crossflow may redistribute low-momentum fluid, deflect existing vortex cores, or weaken their coherence through vortex interaction and mixing. In this interpretation, breaking up a coherent hull-wake structure means reducing its concentrated or correlated impact on the propeller disc; it does not mean eliminating all vorticity. The isolated-foil results demonstrate that the tubercled leading edge can generate the flow structures needed for such an interaction. The hypothesis is that an appropriately positioned hydrofoil uses those structures to reduce adverse inflow non-uniformity and coherent blade-loading fluctuations, potentially improving propulsion performance and reducing underwater noise.

The experiments are consistent with a configuration-dependent response. Vortex interaction can also intensify local turbulence or move a velocity deficit into a more sensitive part of the propeller disc. Any reduction in required power must exceed the hydrofoil's own drag penalty, and smaller flow structures are not necessarily acoustically quieter. The mechanism therefore predicts a benefit only when the strength, trajectory and coherence of the incident wake structures are modified favourably. It is distinct from requiring a net pre-swirl; measurements of pre-swirl devices nevertheless illustrate the value of resolving the propeller-plane velocity field [30].

4.2 Relation to the observed performance and noise response

The two investigations share a qualitative trade-off without measuring the same objectives. In the numerical campaign, increasing amplitude generally lowered both the seven-angle mean L/D and the mean surface p′rms. In the experiments, the W40C20N5 family was quieter on the selected-band average than its smooth counterpart but had a mean DPR of 19.32 mm/rev, below the bare-hull reference. Conversely, a smooth foil, P170W40C40N0, combined a relatively high DPR with a slightly lower mean spectral level. These observations do not support a universal claim that adding tubercles improves propulsion and reduces noise simultaneously.

The pressure-fluctuation maps also show why reduced separation is not a sufficient noise criterion. At moderate incidence, the changing separation pattern coincides with a high surface-average fluctuation level; at 25°, extensive separation coexists with a lower average but locally high values. Radiated sound depends on the frequency content and coherence of the source distribution, not only its RMS amplitude [23,24]. In the ship experiment, the hydrophone additionally samples the coupled system, including

machinery and near-field hydrodynamic contributions. Thus, a decrease in numerical foil p′rms cannot be interpreted as the cause or magnitude of a measured reduction in Lp at a selected experimental frequency.

The opposing acoustic effects of five tubercles at C = 20 and 40 mm reinforce the importance of the interaction geometry: for W = 40 mm, the selected-band mean changes relative to smooth foils were −1.85 and +1.17 dB, respectively. Chord, span and tubercle spacing affect the generated structures, while mounting position sets their development distance before the propeller. These changes could determine whether the foil disperses an adverse hull-wake structure or introduces additional unsteadiness. The absence of a statistically significant mounting-position effect does not establish that the local wake is unchanged. Moreover, the isolated-foil calculations and ship experiment use different sections, Reynolds numbers and inflow conditions, so the numerical structures provide a physical basis for the hypothesis rather than a direct simulation of the observed ship response.

4.3 Future work

A decisive test would compare the bare hull, a smooth hydrofoil and favourable and adverse tubercled configurations at matched operating conditions. Time-resolved velocity measurements or coupled hull–hydrofoil–propeller calculations should track the hull-wake vortices through the hydrofoil region to the propeller plane. Changes in vortex circulation, core trajectory, coherence and axial-velocity deficit would establish whether the foil weakens or redirects the original structures. These changes should then be related to blade-load spectra and to thrust, torque and delivered power; acoustic measurements must distinguish radiated sound from local hydrodynamic pressure.

Resolving this interaction requires a more detailed turbulence treatment in CFD. Pena et al. [37] showed that turbulence-model choice changes the resolved full-scale wake structures and propeller-plane velocity field; the review by Pena and Huang [39] explains why scale-resolving approaches are valuable for unsteady ship-flow and noise problems. Huang et al. [40] further demonstrate that model-scale numerical guidance cannot simply be transferred to full-scale boundary layers. These studies support the required verification strategy, and have the potential to further establish vortex disruption by the present hydrofoil.

5 Conclusions

This study combines isolated-hydrofoil CFD with ship-model experiments to examine how leading-edge tubercles restructure flow and how upstream hydrofoil installations affect vessel advance and underwater pressure spectra. The computational and experimental investigations provide complementary evidence at different geometries and Reynolds numbers, rather than a matched validation pair.

The CFD campaign resolves counter-rotating streamwise structures and incidence-dependent separation. Across the 31 sampled tubercled geometries, the seven-angle mean lift-to-drag ratio and surface pressure-fluctuation measure are positively associated (Spearman $\rho = 0.70$), with amplitude accounting for much of that association. Lower pressure fluctuations therefore do not imply improved foil performance. The result is comparative within the tubercled family and remains subject to turbulence-closure and sampling uncertainty.

The experiments show substantial geometry and frequency dependence. Across 30 hydrofoil configurations and 147 runs, the largest observed single-band reduction was 7.03 dB and the highest configuration-mean DPR was 22.03 mm/rev, 7.8% above the bare-hull reference. These extrema occur as separate outcomes. The 13-band mean spectral-level differences ranged from −1.07 to +3.17 dB, and no configuration demonstrated a consistent advantage in both measures across all selected bands.

Tubercle effects are conditional on the underlying foil geometry. For W = 40 mm, adding five tubercles changed the mean spectral level relative to smooth foils by −1.85 dB at C = 20 mm but +1.17 dB at C = 40 mm. The quieter short-chord family also had lower DPR than the bare hull. The combined findings support joint assessment of hydrodynamic and acoustic objectives rather than selection based on a single best-performing frequency or configuration.

The proposed mechanism is that hydrofoil-generated vortices and crossflow interact with coherent hull-wake structures before they enter the propeller. Favourable interaction could weaken, disperse or redirect concentrated wake disturbances, reducing adverse inflow non-uniformity and unsteady blade loading. This offers a physical explanation for potential propulsion and noise benefits, while also allowing penalties when the hydrofoil adds drag or amplifies unsteadiness. The present measurements establish changes in DPR and local pressure spectra, and future work is proposed to directly demonstrate hull-vortex disruption or improved propulsive efficiency. Matched-configuration flow measurements, thrust and torque data, and acoustically resolved measurements are also suggested to test the proposed mechanics chain.

Acknowledgements

This work is part of a project that has received funding from the EPSRC UK National Clean Maritime Research Hub (EP/Y024605/1).

Data availability

All data underlying the results are available as part of the article and no additional source data are required.

References

[1] International Maritime Organisation. Guidelines for the reduction of underwater noise from commercial shipping to address adverse impacts on marine life. International Maritime Organization 2014. https://wwwcdn.imo.org/localresources/en/OurWork/PartnershipsProjects/Documents/GloNoise-Library/MEPC.1-Circ.833-7April2014.pdf (accessed August 17, 2026).

[2] International Maritime Organisation. Revised Guidelines for the Reduction of Underwater Radiated Noise from Shipping to Address Adverse Impacts on Marine Life. International Maritime Organization 2024. https://wwwcdn.imo.org/localresources/en/MediaCentre/Documents/MEPC.1-Circ.906-Rev.1%20-%20Revised%20Guidelines%20For%20The%20Reduction%20Of%20Underwater%20Radiated.pdf (accessed August 17, 2026).

[3] American Bureau of Shipping. Underwater Noise and External Airborne Noise. 2024.

[4] International Maritime Organisation. 2023 IMO Strategy on Reduction of GHG Emissions from Ships. International Maritime Organization 2023. https://www.imo.org/en/ourwork/environment/pages/2023-imo-strategy-on-reduction-of-ghg-emissions-from-ships.aspx (accessed August 1, 2026).

[5] Fish FE, Weber PW, Murray MM, Howle LE. The Tubercles on Humpback Whales' Flippers: Application of Bio-Inspired Technology. Integr Comp Biol 2011;51:203–13. https://doi.org/10.1093/icb/icr016.

[6] Wikimedia Commons, 2026. (accessed November 07, 2026).

[7] Watts P, Fish FE. The Influence of Passive, Leading Edge Tubercles on Wing performance. 2001.

[8] Johari H, Henoch C, Custodio D, Levshin A. Effects of leading-edge protuberances on airfoil performance. AIAA Journal 2007;45:2634–42. https://doi.org/10.2514/1.28497.

[9] Fan M, Dong X, Li Z, Sun Z, Feng L. Numerical and experimental study on flow separation control of airfoils with various leading-edge tubercles. Ocean Engineering 2022;252. https://doi.org/10.1016/j.oceaneng.2022.111046.

[10] Wei Z, New TH, Cui YD. An experimental study on flow separation control of hydrofoils with leading-edge tubercles at low Reynolds number. Ocean Engineering 2015;108:336–49. https://doi.org/10.1016/j.oceaneng.2015.08.004.

[11] Wei Z, Zang B, New TH, Cui YD. A proper orthogonal decomposition study on the unsteady flow behaviour of a hydrofoil with leading-edge tubercles. Ocean Engineering 2016;121:356–68. https://doi.org/10.1016/j.oceaneng.2016.05.043.

[12] Wei Z, Toh JWA, Ibrahim IH, Zhang Y. Aerodynamic characteristics and surface flow structures of moderate aspect-ratio leading-edge tubercled wings. Eur J Mech B Fluids 2019;75:143–52. https://doi.org/10.1016/j.euromechflu.2019.01.001.

[13] Pena B, Muk-Pavic E, Thomas G, Fitzsimmons P. Numerical analysis of a leading edge tubercle hydrofoil in turbulent regime. Journal of Fluid Mechanics 2019;878:292–305. https://doi.org/10.1017/jfm.2019.611.

[14] Miklosovic DS, Murray MM, Howle LE, Fish FE. Leading-edge tubercles delay stall on humpback whale (Megaptera novaeangliae) flippers. Physics of Fluids 2004;16(5):L39–L42. https://doi.org/10.1063/1.1688341.

[15] Rostamzadeh N, Kelso RM, Dally BB, Hansen KL. The effect of undulating leading-edge modifications on NACA 0021 airfoil characteristics. Physics of Fluids 2013;25(11):117101. https://doi.org/10.1063/1.4828703.

[16] Rostamzadeh N, Hansen KL, Kelso RM, Dally BB. The formation mechanism and impact of streamwise vortices on NACA 0021 airfoil's performance with undulating leading edge modification. Physics of Fluids 2014;26(10):107101. https://doi.org/10.1063/1.4896748.

[17] Posa A, Broglia R, Shi W, Felli M. Large eddy simulation of a marine propeller with leading edge tubercles. Physics of Fluids 2024;36(11):115148. https://doi.org/10.1063/5.0239789.

[18] Hansen KL, Kelso RM, Doolan CJ. Reduction of flow induced tonal noise through leading edge tubercle modifications. 16th AIAA/CEAS Aeroacoustics Conference; 2010. https://doi.org/10.2514/6.2010-3700.

[19] Knox B, Dylejko P, Chen L, Skvortsov A. Mapping Noise and Efficiency for Marine Propeller Designs. Proceedings of Acoustics 2016 2016.

[20] Kimmerl J, Abdel-Maksoud M. Visualization of Underwater Radiated Noise in the Near- and Far-Field of a Propeller-Hull Configuration Using CFD Simulation Results. J Mar Sci Eng 2023;11. https://doi.org/10.3390/jmse11040834.

[21] Tani G, Viviani M, Hallander J, Johansson T, Rizzuto E. Propeller underwater radiated noise: A comparison between model scale measurements in two different facilities and full scale measurements. Applied Ocean Research 2016;56:48–66. https://doi.org/10.1016/j.apor.2016.01.007.

[22] International Towing Tank Conference. ITTC - Recommended Procedures and Guidelines. International Towing Tank Conference 2021.

[23] Curle N. The influence of solid boundaries upon aerodynamic sound. Proceedings of the Royal Society A 1955;231:505–14. https://doi.org/10.1098/rspa.1955.0191.

[24] Turner JM, Kim JW. Aerofoil dipole noise due to flow separation and stall at a low Reynolds number. International Journal of Heat and Fluid Flow 2020;86:108715. https://doi.org/10.1016/j.ijheatfluidflow.2020.108715.

[25] Posa A, Broglia R, Shi W, Felli M. Comparison between the acoustic fields of conventional and tubercled propellers. Physics of Fluids 2025;37(2):025118. https://doi.org/10.1063/5.0251584.

[26] Stark C, Shi W, Atlar M. A numerical investigation into the influence of bio-inspired leading-edge tubercles on the hydrodynamic performance of a benchmark ducted propeller. Ocean Engineering 2021;237. https://doi.org/10.1016/j.oceaneng.2021.109593.

[27] Shi W, Rosli R, Atlar M, Norman R, Wang D, Yang W. Hydrodynamic performance evaluation of a tidal turbine with leading-edge tubercles. Ocean Engineering 2016;117:246–53. https://doi.org/10.1016/j.oceaneng.2016.03.044.

[28] Liu J, Hu L, Zhang B, Zhang K, Bi J, Zheng Q. Enhancing ship hydrodynamic performance via machine learning-driven CFD parametric optimization. Engineering Applications of Computational Fluid Mechanics 2025;19. https://doi.org/10.1080/19942060.2025.2565801.

[29] Atlar M, Seo K, Sampson R, Danisman DB. Anti-slamming bulbous bow and tunnel stern applications on a novel Deep-V catamaran for improved performance. International Journal of Naval Architecture and Ocean Engineering 2013;5:302–12. https://doi.org/10.2478/IJNAOE-2013-0134.

[30] Guo CY, Xu P, Han Y, Zhou GL, Kuai YF, Fan YW. Working mechanism of pre-swirl stator based on stereoscopic particle image velocimetry. Ocean Engineering 2021;236:109442. https://doi.org/10.1016/j.oceaneng.2021.109442.

[31] Langtry RB, Menter FR. Correlation-based transition modeling for unstructured parallelized computational fluid dynamics codes. AIAA Journal 2009;47:2894–906. https://doi.org/10.2514/1.42362.

[32] Menter FR. Two-equation eddy-viscosity turbulence models for engineering applications. AIAA Journal 1994;32:1598–605. https://doi.org/10.2514/3.12149.

[33] Kim I-T, Kim C, Kim S-H, Ko D, Moon S-H, Park H, et al. Estimation of the manoeuvrability of the KVLCC2 in calm water using free running simulation based on CFD. International Journal of Naval Architecture and Ocean Engineering 2021;13:466–77. https://doi.org/10.1016/j.ijnaoe.2021.05.004.

[34] Simman. KVLCC2. Simman2020 2020. https://simman2020.kr/contents/KVLCC2.php (accessed June 16, 2026).

[35] Simman. MOERI Tanker KVLCC2. Webmaster@simman2008Dk 2008. http://www.simman2008.dk/kvlcc/kvlcc2/kvlcc2_geometry.html (accessed June 16, 2026).

[36] Montgomery DC. Design and Analysis of Experiments. 9th ed. Wiley; 2017.

[37] Pena B, Muk-Pavic E, Thomas G, Fitzsimmons P. An approach for the accurate investigation of full-scale ship boundary layers and wakes. Ocean Engineering 2020;214:107854. https://doi.org/10.1016/j.oceaneng.2020.107854.

[38] Pena B, Muk-Pavic E, Fitzsimmons P. Detailed analysis of the flow within the boundary layer and wake of a full-scale ship. Ocean Engineering 2020;218:108022. https://doi.org/10.1016/j.oceaneng.2020.108022.

[39] Pena B, Huang L. A review on the turbulence modelling strategy for ship hydrodynamic simulations. Ocean Engineering 2021;241:110082. https://doi.org/10.1016/j.oceaneng.2021.110082.

[40] Huang L, Pena B, Thomas G. Towards a full-scale CFD guideline for simulating a ship advancing in open water. Ship Technology Research 2023;70(3):222–238. https://doi.org/10.1080/09377255.2023.2167537.